An efficacious model for predicting icing-induced energy loss for wind turbines

Lauren Swenson, Linyue Gao, Jiarong Hong, Lian Shen *

St. Anthony Falls Laboratory, University of Minnesota, Minneapolis, MN 55414, USA

HIGHLIGHTS

- We propose a fast and efficacious framework for wind farm icing loss forecasts.
- This approach bridges meteorological icing and turbine icing-induced energy loss.
- This approach reduces data and computation requirements for icing loss forecasts.

ARTICLE INFO

ABSTRACT

The wind industry in cold climates has shown strong growth in recent years, but turbine icing in these regions can cause significant energy loss leading to a reduction in reliability of wind energy. Previous studies on estimating wind turbine icing (WTI) generally rely on complex physical models, and many only model the ice growth itself while failing to correlate ice growth with energy loss. It is the estimation of icing-induced energy loss that is critical for power grid management to cope with energy deficits associated with extreme weather conditions. This study focuses on bridging this modeling gap through developing an efficacious methodology for predicting icing-induced energy losses for wind turbines in cold weather events. Specifically, this study uses measurements of 11 WTI events between 2018 and 2020 from a 2.5 MW wind turbine (Eolos site, University of Minnesota) to create a statistical correlation between meteorological conditions and icing-induced energy loss. Meteorological icing parameters generated from a Weather Research and Forecasting simulation are used as inputs to the model. The model is validated against in-situ data for all events, and against two additional 1.65 MW wind turbines for one event (Morris site, University of Minnesota). When comparing average estimated energy loss to measured loss, it shows a relative mean absolute error of 37% at Eolos and 2.9% at Morris (after power curve scaling). The new model is additionally implemented for 30 large-scale wind farms in the Midwest region of the United States for estimation of WTI energy loss. The method proposed in this study enables fast and accurate prediction of WTI energy loss for wind turbines.

1. Introduction

According to IEA (International Energy Agency) XIX Annex, wind energy in cold climates refers to sites that may experience frequent icing events, temperatures below the operational limits of standard wind turbines, or both [1]. The global installed wind capacity in these cold climates grew from approximately 127 GW in 2015 to an estimated 186 GW by the end of 2020 [2]. The growth of wind farms in cold climates is driven by factors including land availability [3] and greater energy potential associated with high air densities [4]. In the United States, cold regions like the Upper Midwest and the Great Lakes Mid-Atlantic are still heavily reliant on coal-fueled electricity production, which also creates strong economic and public health incentives for increased wind farm development [5]. However, the weather conditions in these regions can lead to ice accretion on turbine structures, causing energy losses [6,7]. Uneven icing on turbine blades changes the dynamic loads on turbine rotors, accelerating part fatigue and possibly triggering shutoff if high vibrations are sensed [8,9]. Even in less severe icing conditions, icing alters the aerodynamic profile of the turbine blades, leading to reductions in efficiency and power generation [10,11].

The fast expansion of wind installments around the globe has highlighted the challenges associated with integrating wind energy into

---

existing power grids [12,13]. Because wind energy is intermittent in nature, a smooth grid integration demands accurate prediction of wind power fluctuations [14]. Accurate power production forecasts help minimize the financial risk to wind farm owners and electricity traders, reduce the cost of wind energy production [13], and increase overall grid reliability [15]. Several wind power forecasting methods exist today to help system operators plan out wind energy commitments and grid scheduling [16]. However, most operational wind farm production forecast systems do not explicitly factor in icing losses or include only an empirical estimate of annual energy loss [17]. These forecasts would not provide sufficient information for use in power grid management of regions heavily impacted by turbine icing, where reductions in annual energy production can reach upwards of 20% at the most severe IEA Ice Class sites [7]. Therefore, an approach that enables fast and robust forecasts of the icing-induced energy loss for wind farms in cold climate regions such as North America, Europe, Scandinavia, and northern Asia is highly desired.

A variety of published methodologies for estimating wind turbine icing (WTI) exist today, utilizing empirical or physical icing models. Up to now, no empirical icing loss model has been developed to forecast individual WTI events and the corresponding energy losses. Existing empirical models can only evaluate the frequency and severity of past icing events using extensive wind turbine measurements and meteorological data [1]. These models can estimate yearly icing production losses but are not useful for day-ahead or event-specific estimations.

In recent years, physical icing models have been developed in conjunction with the numerical weather prediction (NWP) models to investigate detailed icing processes on wind turbine structures. These physical icing models are mainly based on simplified models, such as the Makkonen ice accretion for standard cylinders model [18], and sometimes also include algorithms to correlate the results of the Makkonen model with actual turbine shape [19] and to factor in ablation. One example of a model that accounts for ablation is the IceBlade model, developed at the Technical University of Denmark (DTU), to estimate ice mass on turbines [9,20,21]. Such physical icing models require information such as the liquid water content (LWC), cloud droplet density (CDD), and median volume diameter (MVD), which can only be measured satisfactorily in lab conditions [19].

Current NWP predictions are mainly used to forecast standard meteorological variables like temperature and precipitation, which are then used to estimate non-prognostic variables like MVD for use in the icing model. The lack of in-situ measurements of some icing model inputs (LWC, MVD, CDD) makes the validation of physical models difficult, and the calculation of MVD based on NWP prognostic variables may introduce additional uncertainty. Using mesoscale weather models to predict MVD has shown some promise but is still largely questionable due to the lack of atmospheric MVD measurements [22]. More importantly, such physical icing models tend to be computationally expensive, adding another barrier to their use in real-time energy loss forecasts for wind farms [20,23]. These models also frequently only estimate the presence of ice itself, instead of extending the model to the more operationally useful estimation of icing-induced energy losses.

Most recently, learning-based models for estimating WTI have been a growing area of study. These methods show promise in their forecast quality and adaptability, but are highly dependent on the training dataset used [24,25]. Although methods like using semi-supervised learning [26] or transfer learning [27] decrease the labor required to make training datasets, the models still require large amounts of historical turbine data. In addition, at the time of this writing, only one published methodology extends the learning-based WTI model to a production loss model [24]. Therefore, there is still a gap between the state-of-the-art in turbine icing models and the realistic implementation of icing-induced energy loss models for large-scale wind farm production estimates.

Motivated by the reviews above, the present study focuses on addressing the shortcomings of current icing models that prevent their

widespread implementation. Specifically, this study focuses on overcoming current empirical models' large measurement dataset requirements and their inability to predict specific icing events. It also addresses physical icing models' challenges of input parameters and computational requirements, and learning-based models' dependence on large training datasets. We propose an approach to achieve fast and efficient forecasts of the icing-induced energy loss for wind farms in large regions during specific icing events. Based on the in-situ measurements of a 2.5 MW wind turbine located at the Eolos Wind Energy Research Station at the University of Minnesota, we derive a relationship between meteorological icing (MI) and the WTI energy loss. Integrated with an NWP system, such a statistical correlation model enables forecasts of wind turbine or wind farm energy losses for specific icing events.

To the best of the authors' knowledge, this would be the first published methodology to effectively forecast the icing-induced wind farm energy loss without requiring any information from the wind turbine's historical supervisory control and data acquisition (SCADA) database after initial model development. Furthermore, such an approach only relies on the most-commonly available weather variables derived from the NWP system, including relative humidity (RH), ambient air temperature (T), and precipitation information, instead of LWC, MVD, CDD or other variables that are difficult to validate with in-situ measurements [28]. Due to the simple requirements for the input data, the proposed approach reduces the obstacle of data accessibility associated with large-scale icing forecasts. It also limits the number of highly computationally intensive steps from both NWP and physical icing modeling, to just the NWP.

The methodology in the present study may be of interest to wind farm operators or developers since it introduces, for the first time, a practical and realistic tool for getting the advanced knowledge needed to prepare wind turbines for coming icing events. The presented approach may also be of interest to power system operators who could apply the proposed method to forecast sudden large-scale energy deficits due to icing and use those forecasts to further increase power system integrity.

Following the introduction above, Section 2 of the paper describes the detailed information about the proposed approach. In Section 3, the approach is evaluated for the Eolos site and validated using the two 1.65 MW wind turbines at the Morris site of the University of Minnesota. Section 4 concludes the present study and discusses further research needs in future studies.

2. Methodology

2.1. Overview

Fig. 1 shows a process diagram for this study, which begins with model development, then validation, and finally implementation. The study is conducted by first using the measurements from the SCADA System of the 2.5 MW wind turbine (referred to as Eolos turbine hereafter) at the Eolos Wind Energy Research Station of the University of Minnesota (UMN) to identify historical WTI events. Based on the energy losses in these WTI events and MI variables measured at the site, we establish a statistical relationship between MI and WTI energy loss. Using simulated meteorological conditions from the Weather Research and Forecasting (WRF) NWP model, we estimate the turbine energy loss for the identified icing events at the Eolos site. Then, to verify the broader applicability of the proposed model, we use the two 1.65 MW turbines located at the Morris site at the UMN to perform further validation. Finally, examples of large-scale implementation of this methodology are presented to demonstrate how this approach may be scaled up from individual turbines to full wind farms, and to lead into possible future work involving the validation of large-scale forecasts such as this.

2.2. Field measurement data and icing events

The in-situ measurements of the WTI events used to develop the
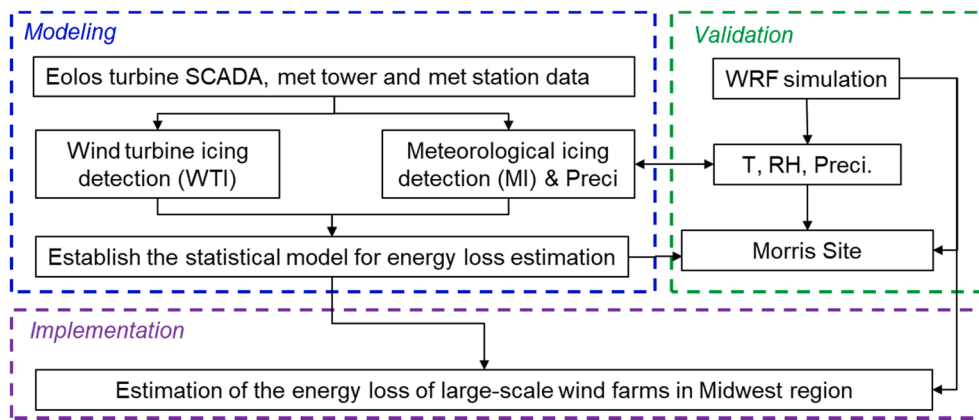
Fig. 1. Flowchart of the model development process used in this study. Inputs include the Eolos database and prognostic variables from the NWP model WRF. These inputs are used for MI, precipitation, and WTI forecasts, which then flows down into the statistical correlation and implementation.
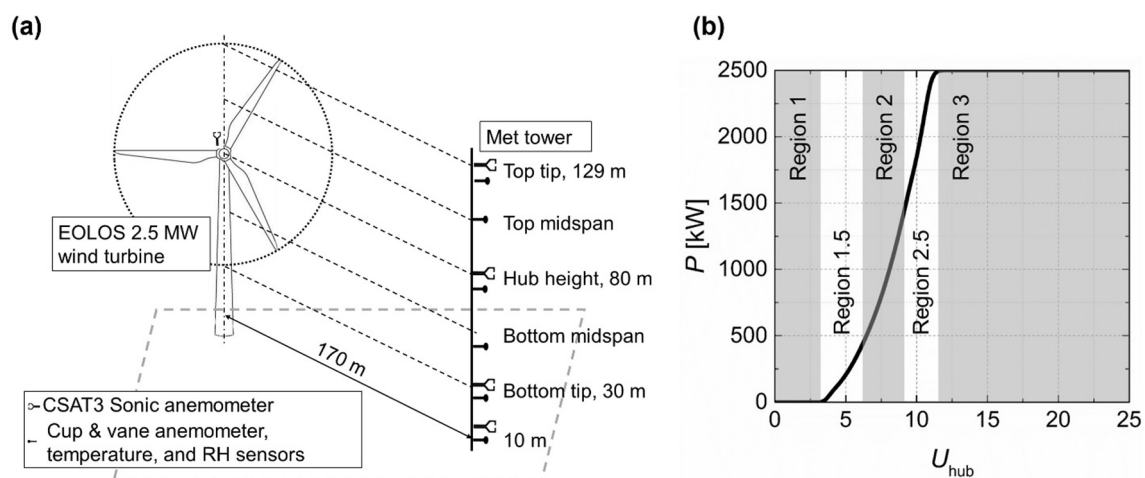

Fig. 2. (a) Schematics of the Eolos Station, including a 2.5 MW wind turbine and a 130 m meteorological tower with associated instrumentation, used as the field station for WTI event measurements. (b) Power curve of Eolos 2.5 MW wind turbine and corresponding operational regions.

statistical model are collected at the Eolos Station in Rosemount, Minnesota, USA. As can be seen in Fig. 4, this site is located at 44°43.693′ latitude, −93°2.8858′ longitude, with a ground elevation of approximately 282 m. As shown in Fig. 2(a), there is a 2.5 MW turbine (Clipper Liberty C96) at this site, which is an upwind three-blade horizontal-axis wind turbine that began operation in 2011 [29]. The turbine has a rotor diameter of 96 m and a hub height of 80 m. The turbine's cut-in wind speed is 4 m/s, rated speed is 11 m/s, and cut-out speed is 25 m/s. The most efficient operating conditions occur when hub-height wind speed (U_{hub}) is within Region 2 (6.9 m/s$\leq U_{hub} \leq$9.2 m/s, see Fig. 2b), generating the maximum power coefficient of 0.472. Region 1.5 is the transition between cut-in speed and Region 2, and Region 2.5 is the transition between Region 2 and rated speed. Historical Eolos station data shows the turbine has a >70% probability of operating in Regions 1.5 through 2.5.

The SCADA system of the turbine records an expansive set of 1 Hz operational and meteorological data. SCADA data used in this study include power production, rotor speed, pitch angle, and wind speeds from an anemometer at hub-height. The turbine is also instrumented with blade and tower sensor systems to measure the structural response at 20 Hz. The Eolos turbine does not have blade heaters or any other active anti-icing mechanisms.

A meteorological tower (referred to as met tower hereafter) located 170 m south of the turbine, also shown in Fig. 2, records surrounding weather data at six vertical levels between the ground and 130 m. This includes wind speed (U) measured by cup and vane anemometers (Met

One, 014A), and T and RH measured by the corresponding sensors (Met One, 083E) with a sampling rate of 1 Hz. Wind speed is also available from sonic anemometers (Campbell Scientific, CSAT3) installed at four heights on the met tower, taking 20 Hz measurements.

In the nine-year period since the Eolos turbine became operational in 2011, turbine icing events are observed between late October and early April of each year. We examine the database from the cold seasons of 2018 through 2020 to select 11 severe WTI events using the 10-min averages of the turbine variables. The selection process for these events includes three steps: clean the raw data, detect periods in the data where icing signifiers are met, and confirm that these periods show icing based on turbine status codes and field observations, as shown in Fig. 3. First, the raw 1 Hz SCADA data of the Eolos turbine from the cold seasons of 2018 through 2020 is averaged in 10-minute periods to filter out the high-frequency fluctuations. The data points affected by curtailment or overheating issues are also discarded using the real power limit information. The Grubbs' test is then used to remove outliers from the dataset.

In the second step, we use the criteria of the MI conditions, i.e., $T < 3\,°C$ [30], and $RH > 85\%$ [28], and a reduction in real power (P)of 15% compared to corresponding no-icing conditions [9,31,32], for the WTI events identification. The no-icing power production is modeled using U_{hub} and the ideal turbine power curve (with a ninth-order polynomial fit). Two additional criteria found to indicate icing events, rotor speed (ω) deficit of over 15% [32] and the occurrence of pitch angle (β) feathering [33], are also used to narrow the selection. Fig. 3(a) shows an
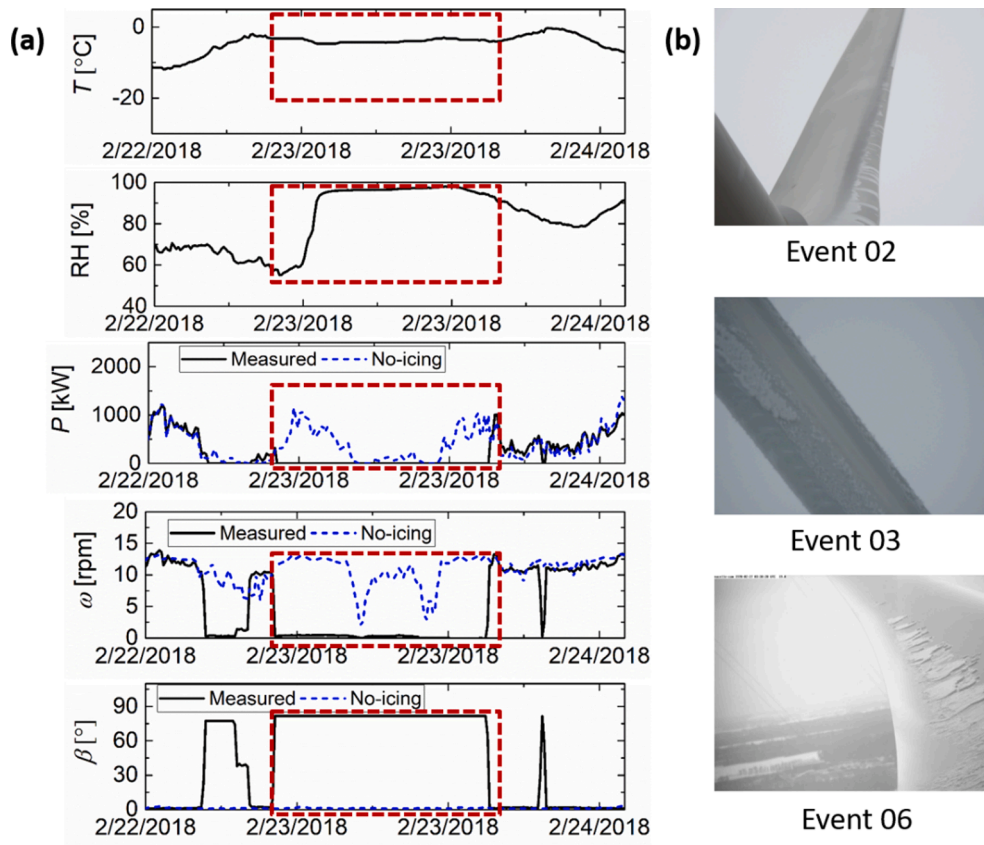
Fig. 3. Field measurements for WTI events at Eolos site: (a) the main features used for the selection of WTI events, shown for Event 3, and (b) the observations of blade icing captured for Events 2, 3, and 6 using cameras.
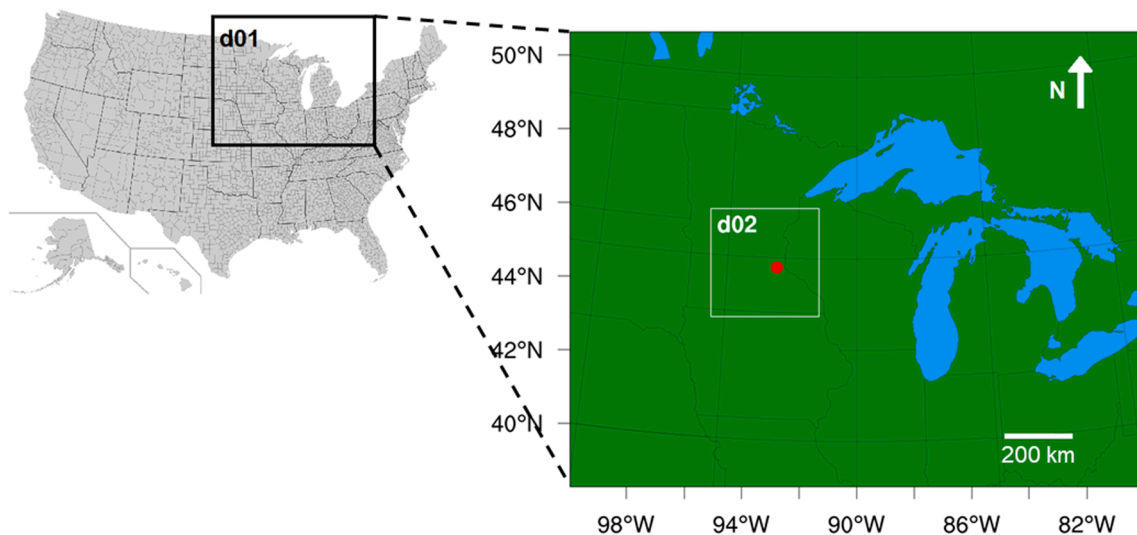

Fig. 4. The WRF simulation domains used for hindcasting of MI parameters: d01 (10 km × 10 km resolution) and d02 (3.33 km × 3.33 km resolution). The red marker indicates the location of the Eolos station used for validation. (For interpretation of the references to colour in this figure legend, the reader is referred to the web version of this article.)

example of these five parameters being identified during an icing event. Events that met these five criteria for a minimum window of four hours are considered with a sliding size of two hours (i.e., twelve consecutive data points representing 10 min each, also used in the literature [31]) for determining WTI events. Note that each chosen period is carefully extended backward and forwards to times that the turbine has detectable power deviations (>30 kW) due to ice accumulation on blades.

The third step in the selection process is to further check and confirm the WTI events are present with the field observations, such as photographs (Fig. 3b), operation logs, or turbine status signals that imply the abnormal turbine operation is not affected by other factors. It should be noted that at the Eolos site, located in flat terrain, the WTI events are mainly caused by precipitation, such as rain or wet snow [7,34], rather than the in-cloud type of icing that usually occurs at mountainous sites

where the cloud base is below the turbine height [34] or with freezing fog [9]. Therefore, we further add precipitation as an additional criterion to further focus the dataset. Precipitation icing will be the focus of the model developed in this study for the Eolos site and the sites with similar geographic features.

The filtering process results in a final selection of 11 events, seen in Table 1. Table 1 lists the length of each icing period as well as the energy loss calculated using operational SCADA data. The average T, RH, and U_{hub} for each event are included. The highlighted rows of Events 2, 3, and 6 indicate the presence of photographic icing evidence. Lack of photographic icing evidence for the other events only means that images of sufficient quality to visually detect icing are not available. The type of precipitation seen in each of the 11 events was added to Table 1 as well. The majority of precipitation seen is snow (*S*), with some events also seeing light freezing rain (*FR*) or a wintry mix (*WM*) of multiple precipitation types. Event 2 saw the most significant periods of *FR* and *WM*.

Additional model validation for this study is performed using data from two Vestas V82-1.65 MW turbines located at a Morris, UMN site. They are located at approximately 45°35.233′ latitude, −95°52.667′ longitude, at an elevation of 347 m. These turbines are used for research at UMN Morris' West Central Research and Outreach Center (WCROC) and to supply energy to the Morris campus [35]. The first wind turbine (WT1) began operation in 2005 and has a 70 m hub height, while the second turbine (WT2) stands 487.7 m further south, began operation in 2011, and has an 80 m hub height. Both turbines have an 82 m rotor diameter, cut-in wind speed of 3.5 m/s, and nominal wind speed of 13 m/s. SCADA data obtained from WCROC includes operating conditions, power production, and weather conditions for each turbine in 10-minute averages. The validation uses datasets for the period from 02/03/2019 5:30 to 02/05/2019 7:20 UTC in addition to long-time precipitation records. Based on the available data from WCROC, the two turbines suffered severe icing-induced energy loss during this period. Note that the period chosen here is different than those studied at the Eolos site due to differences in when severe icing occurs at the two locations.

2.3. Meteorological variables simulated with WRF model

To simulate meteorological conditions at the Eolos site for use in icing models, the WRF Model V4.0 is used for mesoscale weather hindcasting. Nine 5-day simulations are run for the events listed in Table 1, as well as a 7-day simulation to cover both events 8 and 9. All simulations include an additional 12 h in the beginning for model spin-up. Data is output from the model at a 10 min resolution.

Two-way nesting with feedback is used for the domains, with a coarse domain grid resolution of 10 km and fine domain grid resolution of 3.33 km. Fig. 4 shows the locations of the two model domains. A trial simulation of Events 6 and 7 is run with an additional finer domain of 1.11 km resolution, but there is not a significant increase in simulation accuracy to outweigh the increase in computational expense. The Lambert Conformal map projection is used for all domains, as it is known to be best suited to mid-latitude models [36]. As seen in Fig. 4, the model domain covers the Upper Midwest with a focus on Minnesota, Iowa, Wisconsin, and Michigan. The second domain is centered on Minneapolis, Minnesota, and contains the location of the Eolos turbine, whose data is used for model development and validation.

Simulation timesteps of 60 s and 20 s are chosen for the coarse and fine domains, respectively, which follows the recommended timestep (in seconds) of 6 times Δx (in km) according to an NCAR (US National Center for Atmospheric Research) tutorial for WRF [37]. A total of 41 vertical eta levels are selected, with three levels near 130 m, 80 m, and 30 m. Eta levels are concentrated near the ground and grow in spacing towards the model top of 50 hPa. The dataset used to set the initial and boundary conditions for the WRF models is the NCEP Global Tropospheric Final Analysis (NCEP-FNL) from the Global Data Assimilation System [38]. This dataset provides global data on a 0.25° grid at 6-hour intervals. NCEP-FNL is shown to be one of the most accurate analysis datasets and is used widely for initializing data for wind studies [39].

The physics options chosen for this model are listed in Table 2. They include the Rapid Radiative Transfer Model for Global Circulation Models (RRTMG) longwave radiation scheme and the Dudhia shortwave radiation scheme. RRTMG is widely used in weather forecasting models [40] and utilizes lookup tables to describe longwave processes. The Dudhia Shortwave scheme uses downward integration to calculate solar fluxes [40] and is also a common choice for WRF models. The well-established Kain-Fritsch cumulus parameterization is used for the large domain in this study, as it has been shown to perform very well for

Table 2
Physics schemes chosen for use with the WRF mesoscale model.

Physics Option	Physics Scheme
Shortwave Radiation	Dudhia
Longwave Radiation	RRTMG
Land Surface Model	Noah LSM
Cumulus Parameterization	Kain-Fritsch
Planetary Boundary Layer	MYNN2.5
Microphysics Scheme	Morrison, WSM5

Table 1
Selected 11 WTI events by screening the Eolos database from 2018 to 2020.

	WTI					Weather			
Event	Start time [UTC]		End time [UTC]		Duration [h]	Energy loss [kWh]	RH [%]	T [°C]	U_{hub} [m/s]	*Precip.*
1	01/14/18	22:15:00	01/16/18	19:50:47	45.33	3.50×10^4	80.95	-15.03	6.93	*S*
2	02/19/18	13:44:59	02/21/18	8:45:33	43.00	2.57×10^4	87.14	-8.30	6.87	*S, FR, WM*
3	02/22/18	21:35:33	02/23/18	14:37:34	17.17	6.58×10^3	89.46	-3.88	5.43	S
4	12/02/18	7:08:44	12/02/18	18:59:16	12.00	1.05×10^4	87.27	-1.20	10.83	*S*
5	12/27/18	4:45:21	12/27/18	20:15:24	15.67	9.87×10^3	87.60	-4.73	9.14	*S*
6	02/07/19	6:25:00	02/08/19	9:34:59	27.33	1.10×10^4	86.81	-12.91	6.98	*S, WM*
7	02/12/19	19:05:00	02/13/19	13:35:56	18.67	2.18×10^4	84.62	-10.47	8.64	*S*
8	02/20/19	11:06:03	02/21/19	16:32:35	29.17	2.25×10^4	88.15	-7.75	6.98	*S*
9	02/24/19	7:24:22	02/25/19	2:26:35	19.17	2.21×10^4	74.94	-10.04	13.06	*S*
10	01/13/20	20:15:01	01/14/20	7:45:37	11.67	7.18×10^3	90.73	-3.73	6.77	*S, FR*
11	01/18/20	1:17:42	01/19/20	13:48:50	35.00	3.49×10^4	84.00	-11.96	8.23	*S, FR, WM*

wintertime precipitation events, specifically frontal precipitation [41]. No cumulus scheme is used for the nested domain because a cumulus parameterization is generally not needed for grid sizes of <4 km, unless in the presence of sub-grid size isolated convection cells [42,43]. A preliminary sensitivity study performed with various PBL schemes (MYJ, YSU, MYNN2.5) shows that the MYNN2.5 scheme produces the lowest U_{hub} bias and RMSE compared to the Eolos met tower data, as well as the lowest T bias when averaged across 10 m, 30 m, 80 m, and 130 m elevations.

Three microphysics schemes are tested for Event 7: two 6-class schemes with graupel, the New Thompson scheme, and the Morrison 2-moment scheme, as well as one 5-class microphysics scheme with ice, the WSM5 scheme. The 6-class schemes are chosen because of their complex parameterizations of precipitation, while WSM5 is chosen because it has shown comparative performance to the more complex schemes but much shorter computation times [44]. The New Thompson scheme in particular includes predictive precipitation variables for snow, rain, graupel, water vapor, cloud water, and cloud ice [45]. However, the New Thompson scheme is eliminated because it shows a large overestimation of *RH* during a significant period of this simulation. All other events are then simulated twice, once with the Morrison scheme and once with WSM5.

WRF prognostic variables for total precipitation in mm and snowfall in mm are output from the simulations. Graupel is also output from the Morrison microphysics models. In the 11 events simulated, the vast majority of precipitation is in the form of snow. To allow for comparison with the in-situ precipitation observations, the total precipitation values from WRF are converted into a binary. The threshold value for precipitation rates is set at 0.03 mm h^{-1}. This value is consistent with the lightest observable snowfall rate seen in a study of snowfall and visibility [46]. The WRF models for the Morris site validation and large-scale wind farm implementation use the same settings and configurations as for the Eolos site simulation, except that meteorological data is extracted only from the coarse domain. This better facilitates model implementation for multiple wind farms in a large area, without the need for several computationally expensive fine domains. A five-day WRF simulation with 12 h for model spin-up is used for both the validation and implementation scenarios as well.

2.4. Statistical energy loss model

Using the SCADA and in-situ meteorological data of the 11 known Eolos WTI events, a statistical energy loss model is developed. This process is summarized in Figs. 5–8, including identification of the presence of WTI event, estimation of the duration of the event, and evaluation of the turbine energy loss.

First, we need to identify whether there is a chance in the presence of WTI events based on the MI and precipitation information. MI ($T < 3\,°C$, and $RH > 85\%$) and precipitation (*Preci.*) are the prerequisites for the occurrences of WTI events [47], as stated in Section 2.2. Note that the precipitation information is integrated into the modeling with the binary signals, i.e., 0 for no precipitation while 1 for precipitation conditions, including snow (light, regular, heavy, and blowing), freezing rain/drizzle, wintry mix, haze, etc.

Based on the field observations and measurements of WTI events at the Eolos station from 2018 to 2020 winters, we have found that those periods of time with only one factor met tend to lead to no presence of WTI events, as shown in Fig. 5(a). In addition, if the total duration of the overlap period between MI and *Preci.* is less than four hours, it is also unlikely to have appreciable influence on turbine operation and power output [31] and thus those periods can also be grouped into no presence of WTI event category. Due to fluctuating T and RH, conditions may fall below the MI threshold for brief periods, or gaps in an otherwise long MI period. As shown in Fig. 5(b), the two MI periods are suggested to be merged if the gap is less than two hours and this gap period has a precipitation record, which is also used in the literature [31]. If the gap is larger than two hours, only the MI period that also shows precipitation is considered. This criterion allowed a simple temporal relationship among WTI, MI, and precipitation to be developed.

Second, the duration of turbine icing is highly correlated with the turbine energy loss due to the increasing ice accumulation on the turbine structures over time [28]. Therefore, we use the duration of WTI to quantitatively relate the meteorological conditions to wind turbine energy losses. However, the duration of WTI differs from those of the MI or *Preci.* periods, primarily due to the delay of ice accretion over the turbine structures and the slow natural melting and sublimation processes of the ice structures. As shown in Fig. 6, the strongest indicator of WTI start-time is found to be related to when both MI and *Preci.* first occurred together based on the measurements of 11 WTI events at the Eolos site. WTI begins a certain period, C_1, after the onset of MI and *Preci.*

$$\widehat{t}_{WTI,start} = t_{preci.\&MI,start} + C_1 \tag{1}$$

where $C_1 = 4h$ based on the Eolos dataset used in this study with a 95% confidence interval of 1.48 h. The strongest indicator of WTI end-time is related to the end of precipitation only. Some multiple of the duration of MI and *Preci.*, C_2, is added to the precipitation end-time to get the time of WTI end to cover the slow natural melting and sublimation period of iced turbine blades:

$$\widehat{t}_{WTI,end} = C_2 \left(t_{preci.,end} - t_{preci.\&MI,start} \right) + t_{preci.,end} \tag{2}$$

where $C_2 = 0.1$ based on the Eolos dataset used in this study with a 95%

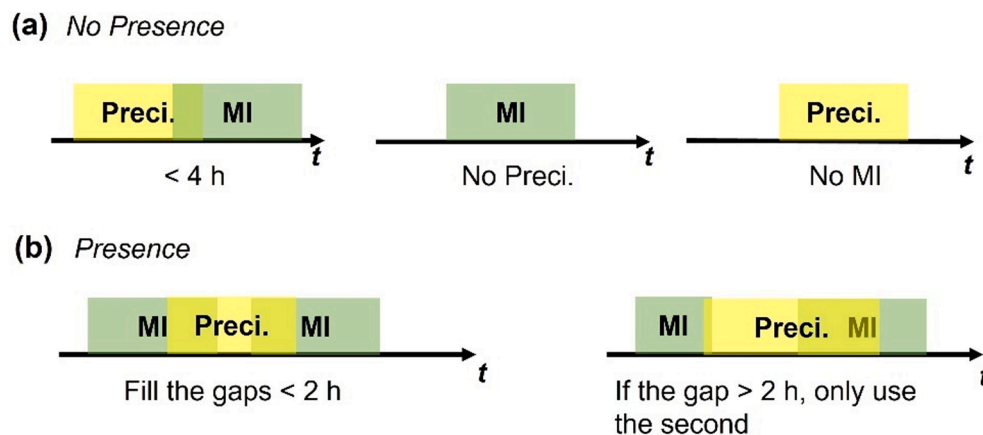**(a)** *No Presence*

(b) *Presence*

Fig. 5. Estimation of the presence of potential WTI events based on related weather variables from in-situ data of the Eolos turbine. (a) Three types of cases tend to infer no presence of potential WTI event, and (b) two conditions intend to infer the presence of potential WTI event.
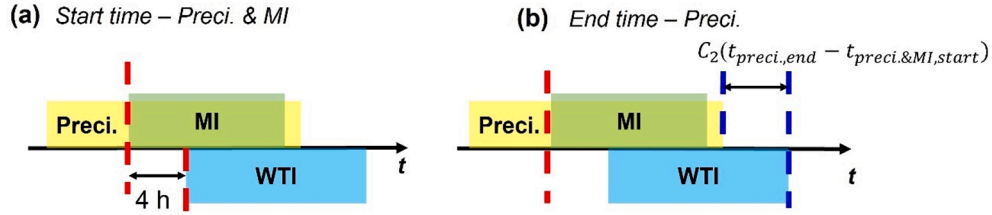
Fig. 6. Estimation of the WTI event duration based on the in-situ data of the Eolos turbine.
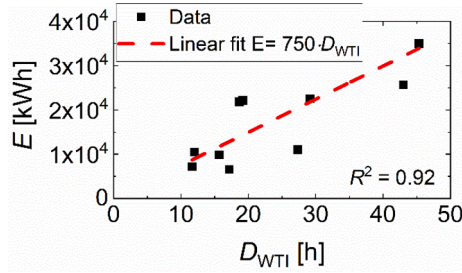

Fig. 7. Relationship between WTI event duration and icing-induced energy loss experienced for the Eolos turbine.
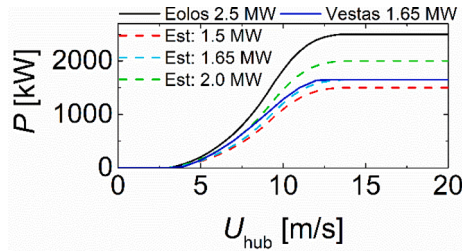

Fig. 8. Scaling to turbines with different capacities using the 2.5 MW Eolos power curve.

confidence interval of 0.0591. The WTI duration is then calculated using the icing start and end times:

$$\widehat{D}_{WTI} = \widehat{t}_{WTI,end} - \widehat{t}_{WTI,start} \tag{3}$$

After Eq. (1) through (3) are used to determine the duration of WTI, a relationship between icing duration and energy loss is found based on the energy loss (E) and WTI event duration (D_{WTI}) for the 11 events listed in Table 1, shown in Fig. 7.

A linear regression is applied to the WTI durations and known Eolos energy loss datasets. The resulting linear fit based on the Eolos data has a slope of 750 kWh/h and a coefficient of determination of $R^2 = 0.92$:

$$\widehat{E} = C_3 \cdot C_4 \cdot \widehat{D}_{WTI} \tag{4}$$

where $C_3 = 750$, and $C_4 = scaling\,factor$. Because this relation depends on empirical energy loss data from the Eolos turbine, it must be scaled before using for turbines with different capacities. To account for this, the maximum rated power of the chosen turbine (P_{max}) and the maximum rated power of the Eolos turbine ($P_{max,Eolos}$) are factored into the equation as $C_4 = P_{max}/P_{max,Eolos}$. The power curves between two variable-speed and variable-pitch regulated turbines (i.e., most used utility-scale wind turbines) are quite similar with close cut-in, rated, and cut-out wind speeds, and thus they can be directly scaled as C_4. Fig. 8 shows the scaling process for a Vestas 1.65 MW turbine, resulting in an error of 2.8% when comparing the calculated power curve to the known power curve for this turbine.

2.5. Model evaluation

The simulation accuracy of the meteorological variables (i.e., T, U, RH, and $Preci.$) with the WRF model has an essential influence on the final energy loss forecast results. The simulation results of the variables (T, U, RH) are evaluated against observed meteorological variables using mean absolute error (MAE), as defined in Eq. (5).

$$MAE = \frac{1}{n}\sum_{i=1}^{n}|y_i - \widehat{y}_i| \tag{5}$$

where y_i represents the measured values, $\widehat{y}_i$ represents the simulation outputs, and n is the number of data points compared. For the variable $Preci.$ with binary information of 1 and 0, accuracy is used to evaluate the simulation results, as given in Eq. (6), the ratio of correct estimations over the number of total estimations.

$$Accuracy = \frac{TT + FF}{TT + FF + TF + FT} \times 100\%. \tag{6}$$

where TT represents the number of true-true events (where both the simulation and observation data point indicate precipitation), FF represents the number of false-false events (where precipitation is seen in neither data point). TF and FT represent the number of true–false events (false alarm) and false-true events (missed prediction), respectively. Eq. (6) is also used to calculate the accuracy of icing event predictions for the statistical WTI model itself.

For the other parameters, e.g., energy loss, relative mean absolute error (RMAE) is used for characterizing the error in the estimates by comparing with measurements, as shown in Eq. (7).

$$RMAE = \frac{1}{n}\sum_{i=1}^{n}|y_i - \widehat{y}| \bigg/ y_i. \tag{7}$$

3. Results and discussion

3.1. Validation of meteorological model

Fig. 9 shows a sample time series of relevant meteorological variables from the two WRF simulations and the Eolos measurement dataset. The data shown in Fig. 9 is from Event 3 at the 80 m elevation. Although the initial evaluation was performed at three heights (30 m, 80 m, and 130 m to represent the full vertical range of the turbine blades), there was not a significant change in T or RH across these elevations during the selected icing events, so only validation at hub-height is shown here. In general, the modeled data follows the overall trends of the measured data. The only notable deviations in this event are the early onset of high RH and early precipitation predictions seen in the modeled data. As temperature is below 3 °C for the entire period, it can be expected that using this data to feed the statistical energy loss model would result in a slight overestimate of icing losses.

It can be seen, most notably in the U_{hub} time series of Fig. 9, that the model cannot accurately capture all the high-resolution variability seen in the measured data. This may be due to multiple factors, including that the input dataset used for the WRF model has only a 6 h resolution, and that WRF is primarily designed for mesoscale NWP so cannot always
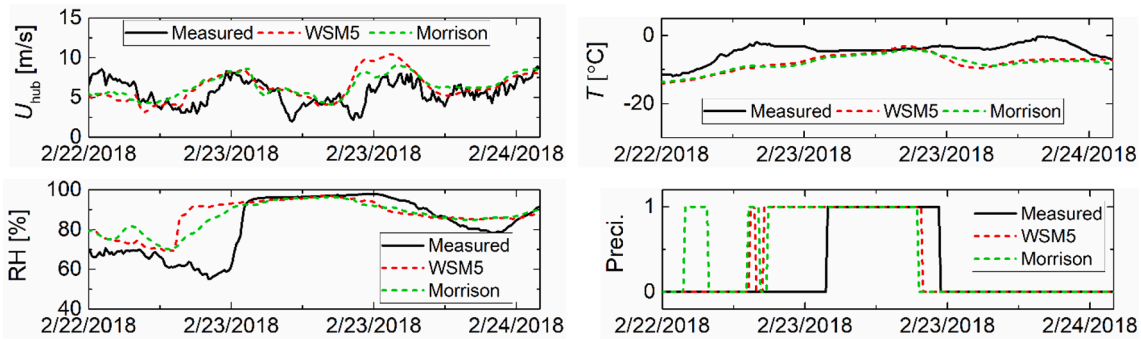
Fig. 9. Example time series of evaluation results for the WSM5 and Morrison WRF models at 80 m. Event 3 simulation outputs and in-situ Eolos measurements are compared for the four meteorological parameters relevant to MI.

capture the microscale processes that lead to these very fast changes. Using higher-resolution terrain data or a smaller WRF domain resolution may help improve the capture of these features. A shorter integration timestep is another method that may in some cases have an improvement on the high-frequency response of the model.

Fig. 10 shows the variation in errors for the modeled meteorological variables across all 11 icing events at the Eolos station. Meteorological data from both the WSM5 and Morrison WRF simulations are validated against in-situ data at hub-height to compare the quality of the two simulations. Eq. (5) is used to calculate the MAE of *U*, *T*, and *RH*, and Eq. (6) is used to calculate accuracy of the precipitation estimate. The MAE's shown in Fig. 10 are on the same order of magnitude as those seen in studies using WRF models of the Central United States for windspeed [48,49], temperature [49], and relative humidity [50].

The performance of modeled icing events shown in Fig. 10 varies between the microphysics scheme used, the icing event, and the prognostic variable in question. Whether the WSM5 or Morrison model performs better is not consistent across events or variables, and in general, there is a larger difference in errors between events than between the two models of a single event. Therefore, data from both models is used to perform icing loss estimations. Variation in errors between icing events when using the same WRF model may be due to different atmospheric conditions or processes present in different events. For instance, Event 8 is unique in that its observational record showed long periods of high winds and blowing snow, which is counted as precipitation as it could lead to turbine icing similar to that caused by active snowfall. However, the standard WRF model does not take blowing snow into account [51], possibly leading to the low accuracy of the precipitation estimation in Event 9.

3.2. Performance evaluation based on Eolos site

To evaluate the performance of the proposed statistical model, we use 1-year data from the Eolos database (1-hour resolution, in 2019) to determine the model's accuracy in predicting WTI event occurrence over a full year. In this year, the availability of data is 97%, i.e., 8528 out of the total number of hours of 8760 in one year. The overall accuracy of the prediction is 99.3% (*TT*: 2.7%, 230 h/year, and *FF*: 96.6%, 8238 h/year). The false alarm rate (*TF*) is 0.3% (i.e., 26 h/year), while the missed prediction (*FT*) rate is 0.4% (i.e., 43 h/year). Such results suggest that our model could work well during routine daily turbine operations.

Feeding the statistical energy loss model with meteorological data from the WRF simulation instead of the in-situ Eolos data allowed the NWP and statistical models to be integrated. The meteorological data used came from the WSM5 and Morrison microphysics scheme WRF runs, as well as the averaged data between both runs. Energy losses from the model and the Eolos database for each event are shown in Fig. 11. The estimated energy losses based on the Morrison simulation dataset are larger than those estimated with the WSM5 dataset in eight of the eleven events. Because the same statistical energy loss model was applied to all three meteorological datasets, the spread in energy losses must be due to differences in the predicted meteorological variables. Event 8 showed the largest spread between the WSM5 and Morrison estimations. The validation of the simulation data in Section 3.1 also shows Event 8 had the largest difference in estimated *RH* between the two simulations. The WSM5 simulation underestimates *RH* on average for this event, while the Morrison simulation overestimated it, contributing to the large spread in energy loss predictions.

As shown in Fig. 11, Events 3, 4, and 10 had the overall smallest errors in energy loss estimates. The simulations of Events 4 and 10 showed the lowest MAE in *T* estimations, but otherwise, the simulation
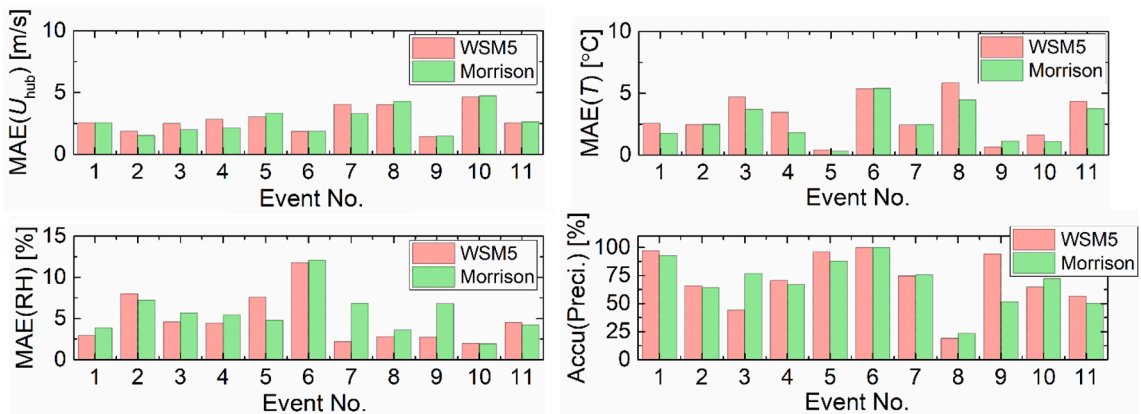

Fig. 10. Validation results for the mesoscale model at 80 m after comparison to measurement data, including MAE and accuracy for four prognostic model variables for each of the 11 icing events. Data is shown from WRF models using both the WSM5 and Morrison schemes.
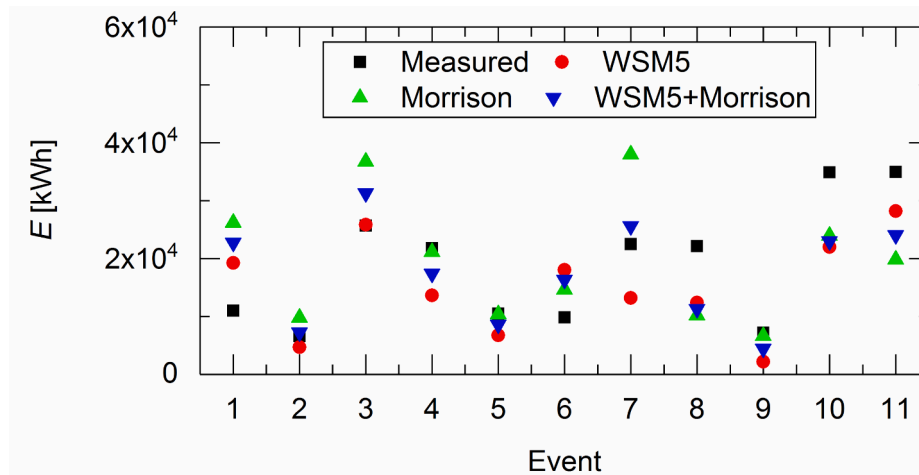
Fig. 11. Comparison of modeled and actual energy losses for 11 icing events at the Eolos turbine. Modeled losses are calculated using prognostic meteorological variables from two WRF models at the 80 m height, as well as the average from the two models.

accuracy of these events did not differ largely from the average simulation accuracy across events for *RH* or precipitation. These three events do, however, represent some of the lowest measured energy losses, naturally lending to smaller errors in predicted energy loss. Using relative error in Fig. 12 to better illustrate the errors across events, the quality of estimations for Events 3, 4, and 10 no longer appear significantly better than the quality of most other estimations. Event 6 now stands out as having the highest relative estimation errors. A spread of both positive and negative errors is also more clearly visible in Fig. 12, with no consistent bias for either the WSM5 or Morrison WRF models.

When considering all icing events together, the RMAE for the energy loss estimate using the WSM5 dataset and the Morrison dataset are 42% and 44%, respectively. The averaged WSM5 + Morrison dataset shows a lower RMAE, at 37%, and thus is used in the following forecasts. For this study, the largest contributions to RMAE come from Event 6 for the Morrison and WSM5 + Morrison datasets and Event 5 for the WSM5 dataset. The high relative error of these events can partially be attributed to their low measured energy losses, in comparison to Event 11, which shows high absolute errors but also high measured energy loss. For the remainder of this study, energy loss estimates are calculated using the averaged WSM5 and Morrison WRF simulation outputs. There is no data available from the state-of-the-art studies related to the icing loss prediction during a single icing event. The current information

available in literature [9] about the wind farm annual energy production (AEP) estimation with consideration of icing related loss shows a RMSE in the approximate range of 3% to 23%, which could significantly smooth out the uncertainties in the predictions for single icing events.

3.3. Performance validation based on Morris site

SCADA power and operational data from the two Vestas V82 1.65 MW turbines at the Morris, UMN site is used to find the measured energy loss (E_{mea}) during the WTI period from 02/02/2019 23:30 to 02/05/2019 1:20 CST (local time) for the first turbine (WT1). The second turbine (WT2) exhibits a 20 min offset in the WTI duration, i.e., two data points of the 10-min averages, suggesting negligible differences between

Table 3
Energy losses at the two wind turbines, and the average energy losses between the two.

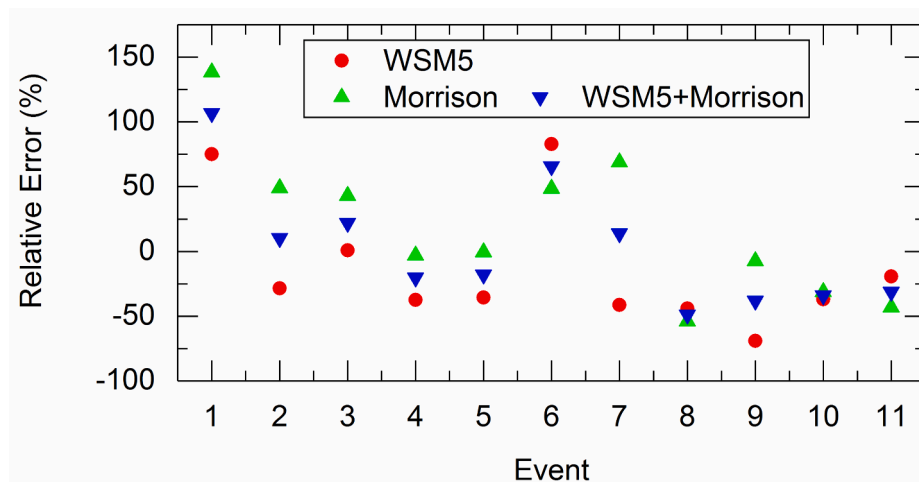|	$\widehat{E}$ [kWh]	$E_{mea,WT1}$ [kWh]	$E_{mea,WT2}$ [kWh]	$\overline{E}_{mea}$ [kWh]
Vestas power curve	–	3.67×10^4	3.88×10^4	3.78×10^4
RMAE (Vestas)	–	1.3%	7.0%	4.4%
Scaled power curve	3.61E04	3.61×10^4	3.40×10^4	3.62×10^4
RMAE (Scaled)	–	6.1%	0.2%	2.9%

Fig. 12. Relative errors calculated for each modeled Eolos icing event in comparison to the known energy losses. Calculations are based on energy losses from Fig. 11.

the two turbines. As shown in Table 3, in general, the proposed method has a good prediction for the Morris turbines with an average error of <5%. Specifically, because the two turbines are located at the same site with the same modeled meteorological data, they exhibit the same estimated energy loss of $\widehat{E} = 3.61 \times 10^4$ kWh. This is based on the scaled power curve found using the Eolos power curve and the scaling factor of $P_{max,Eolos}/P_{max,Vestas}$. The RMAE of average estimated energy loss for the two turbines decreases from 4.4%, when using the Vestas' power curve for the estimation, to 2.9% when using the scaled power curve.

Such a trend further indicates that the scaled power curve works well, which allows the forecasts for the wind farms with unknown power curves. In addition, the two turbines have a small difference (<6%) in the energy loss, i.e., $(E_{mea,WT1} - E_{mea,WT2})/\overline{E}_{mea}$, further indicating the proposed method could be used for wind farm applications with multiple turbines. Note that the low RMAE observed in this WTI event at the Morris site, compared with the 11 events in the Eolos site, is mainly associated with its longer duration and higher energy loss.

3.4. Large-scale model implementation

An application of this model is shown for a selection of 30 wind farms across the Midwest, USA, in the period of 02/21/2018 12:00 to 02/27/2018 00:00 UTC, the same simulation period used in the Eolos WTI Event 3. Fig. 13 shows the location and rated capacity of each wind farm in the dataset. They are also listed in Appendix A. Wind farms with at least 30 turbines are pulled from the Wind Turbine Database [52] to create this dataset. Wind farms are selected from Minnesota, Iowa, Wisconsin, and Michigan to create a geographically diverse sample of farms in areas with similar climate and topology as the Eolos and Morris sites. In cases where a wind project is listed in the database as multiple adjacent wind farms (i.e., Storm Lake I and Storm Lake II), the wind farms are combined into a single data point for use here.

The meteorological data at each of these sites is extracted from the WRF simulation data during the selected period. The data is then fed into the statistical energy loss model and scaled for the average turbine capacity of each farm. This results in the estimated icing energy loss for the average turbine in a farm ($\widehat{E}$), which is scaled up to obtain energy loss for the entire wind farm ($\widehat{E}_{WF}$):

$$\widehat{E}_{WF} = n_{WT}\widehat{E} \tag{8}$$

where n_{WT} is the number of wind turbines in a wind farm. Most of the 30 wind farms are found to experience two turbine icing events during this period, except for the Pine River wind farm, which shows no icing, and the Gratiot County, Tuscola Bay, and Michigan Wind II wind farms
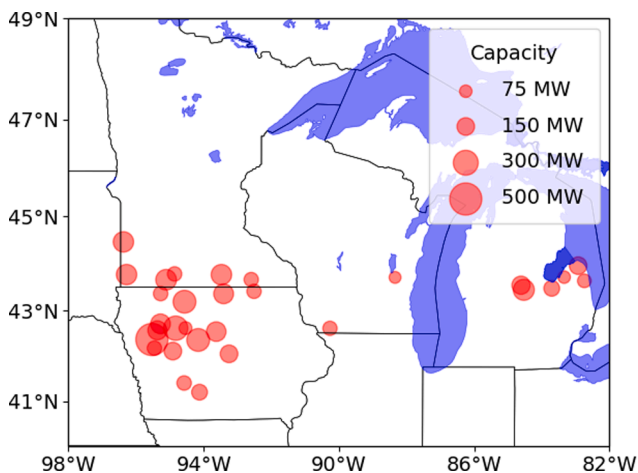

Fig. 13. Map of the 30 wind farms in the Midwest U.S. selected for model implementation, with markers scaled to their rated capacities in MW [52].

which each shows one icing event. The total icing loss per period is then calculated for each wind farm:

$$\widehat{E}_{WF,period} = n_{WT}\sum_{i=1}^{k}\widehat{E} \tag{9}$$

where k is the number of icing events seen in the period for a given wind farm. The overall energy loss of the 30 wind farms is estimated to be 21 GWh, or 9% during the selected week. Fig. 14 shows how this breaks down across each individual wind farm and by state.

This implementation study shows an estimate of icing-induced energy losses for wind farms over a large geographic region. Real energy loss data from these wind farms is not publicly available to judge the accuracy of these estimations, but in future work verification could be performed to test the applicability of this model for the large-scale use case. The methodology used shows promise for its speed and simplicity, pending verification results to solidify its usefulness. The method only requires the number and capacity of wind turbines in the wind farm to conduct the forecasts of the icing-induced energy loss. There is no need to have the wind turbine SCADA data, wind turbine power curve, or other detailed information. With the meteorological data extracted from the WRF simulations (5-day Midwest region run, 100–300 CPU hours), we can expect the prediction results from the statistical model in a couple of minutes.

For new wind farms in the planning phase, where complete in-situ icing data is not yet available or a large geographic area needs to be studied, this methodology may be able to be adapted for use in hindcasting icing effects. As this method does not necessarily rely on in-situ data, after necessary analysis of the model's accuracy is performed for the scenario and region of interest, estimated icing losses for chosen events could be modeled for anywhere in the domain. Such information about the icing effect on wind farm AEP could provide insights to the wind farm operators whether the wind farm needs to equip with icing protection systems. For existing wind farms, the icing-induced energy loss model could be used for correction of the currently used days-ahead power forecasts based on the hourly meteorological forecasts from the NCEP's operational High Resolution Rapid Refresh system [53,54]. Because of the speed and simplicity of the statistical correlation method, icing loss estimates could be provided immediately once the weather forecasts are imported. Further work and validation of this process would need to be performed to ensure the added uncertainty of using a weather forecast does not overcome the prediction capabilities.

4. Conclusions

In the present study, we propose a method to enable fast and efficacious forecasts of the icing-induced energy loss for wind turbines. With numerical weather prediction model Weather Research and Forecast (WRF) simulations, the meteorological icing variables are derived to identify the potential wind turbine icing events and corresponding energy losses related to the precipitation icing. A statistical model derived from the in-situ field measurements of a utility-scale wind turbine fills the gap between the meteorological icing and the wind turbine icing event and the corresponding energy losses. This method is implemented and evaluated for three turbines at the Eolos and Morris sites of the University of Minnesota. When using a combination of two microphysics schemes to generate meteorological data from WRF simulations, estimated energy losses at the Eolos and Morris sites show the estimation errors between 0.2% and 37% for 12 icing events.

This method of estimating icing losses is efficient, relatively inexpensive computationally, and shows promising application potentials for wind farms. This method only requires the meteorological variables, i.e., temperature, relative humidity, and precipitation, as well as wind turbine capacity and the number of wind turbines in the wind farm for the forecasts. It is not required to know the detailed wind turbine power curve and wind turbine SCADA data, which indicates that the model may be easily adapted to icing-induced energy loss forecasts in large
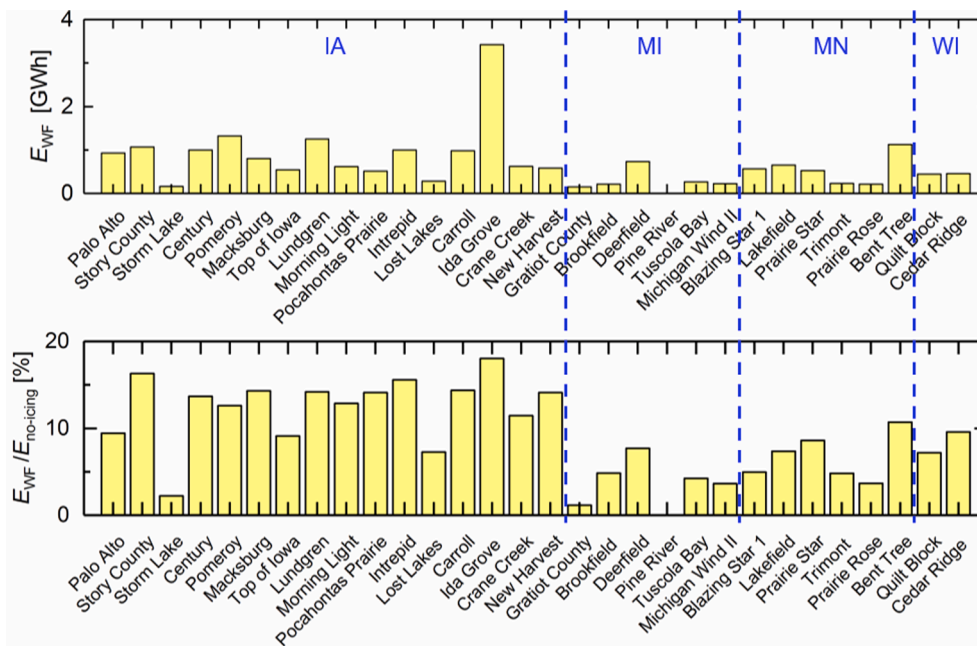
Fig. 14. Estimated total energy loss for each of 30 modeled wind farms, broken into sections based on wind farm location. Percentage icing losses are based on the standard capacity of each wind farm.

areas. During the planning phase of a wind farm, this method could enable energy loss hindcasting based on widely available meteorological datasets, which would be a useful tool to determine whether turbines at the site need to be equipped with icing protection systems. For existing wind farms, this method could provide the forecast results of potential icing events, and such information can bring insights to power market dispatching and thus increase the integrity of the power grid.

Because of WRF's capabilities in near-term forecasting of meteorological variables, this method may be best suited to day-ahead operations. If the statistical modeling component of this method were to be integrated into the existing wind and weather forecasting methods used by Independent System Operators (ISOs) across the U.S., it may provide more educated inputs for the settling of marginal electricity costs during day-ahead market clearing. Consideration of icing effects in ISO production forecasts could lead to improvements of reliability and cost efficiency of unit commitments.

The uncertainties of the proposed method mainly arise from errors in the WRF simulations, i.e., the inputs of the statistical model, and the simplicities in the statistical model. For example, the statistical model assumes different wind turbines in a wind farm tend to experience the same energy losses. For large-scale wind farms, the differences among turbines in terms of turbine healthy conditions, the wake effects of upstream turbines to downstream turbines, and other factors may add to the uncertainties in the forecast results. In addition, this model is developed specifically for precipitation icing situations, suitable for wind farms located in flat terrains. It should be cautioned that this model

was not designed to be implemented for mountainous wind farm sites or high elevation sites where in-cloud icing is predominant.

CRediT authorship contribution statement

Declaration of Competing Interest

The authors declare that they have no known competing financial interests or personal relationships that could have appeared to influence the work reported in this paper.

Acknowledgements

Appendix A. A list of 30 wind farms in the Midwest United States shown in Fig. 13 [52].

	Wind Farm	State	County	Year	WF Cap. [MW]	Number of WT's	Avg. WT Cap. [kW]
1	Palo Alto	IA	Palo Alto County	2019	250	125	2000
2	Story County	IA	Story County	2008	150	100	1500
3	Storm Lake	IA	Buena Vista County	1999	188.25	251	750
4	Century	IA	Hamilton County	2005	185	135	1500
5	Pomeroy	IA	Pocahontas County	2008	284.9	183	1500
6	Macksburg	IA	Madison County	2014	119.65	51	2300
7	Top of Iowa	IA	Worth County	2001	189.8	147	900

(*continued*)

	Wind Farm	State	County	Year	WF Cap. [MW]	Number of WT's	Avg. WT Cap. [kW]
8	Lundgren	IA	Webster County	2014	251.02	107	2300
9	Morning Light	IA	Adair County	2012	101.2	44	2300
10	Pocahontas Prairie	IA	Pocahontas County	2012	80	40	2000
11	Intrepid	IA	Buena Vista County	2004	175.5	122	1500
12	Lost Lakes	IA	Dickinson County	2009	100.65	61	1650
13	Carroll	IA	Carroll County	2008	150	100	1500
14	Ida Grove	IA	Ida County	2019	501.06	215	2500
15	Crane Creek	IA	Howard County	2009	99	66	1500
16	New Harvest	IA	Crawford County	2012	100	50	2000
17	Gratiot County	MI	Gratiot County	2012	212.8	133	1600
18	Brookfield	MI	Huron County	2014	74.8	44	1700
19	Deerfield	MI	Huron County	2017	149	72	2000
20	Pine River	MI	Isabella County	2019	161.3	65	2500
21	Tuscola Bay	MI	Saginaw County	2012	120	75	1600
22	Michigan Wind II	MI	Sanilac County	2011	90	50	1800
23	Blazing Star 1	MN	Lincoln County	2020	200	100	2000
24	Lakefield	MN	Jackson County	2011	205.5	137	1500
25	Prairie Star	MN	Mower County	2007	99	60	1650
26	Trimont	MN	Jackson County	2005	100.5	67	1500
27	Prairie Rose	MN	Rock County	2012	199.92	119	1600
28	Bent Tree	MN	Freeborn County	2011	201.3	122	1600
29	Quilt Block	WI	Lafayette County	2017	98	49	2000
30	Cedar Ridge	WI	Fond du Lac County	2008	67.65	41	1650

References

[1] Laakso T, Baring-Gould I, Durstewitz M, Horbaty R, Lacroix A, Peltola E, et al. State-of-the-art of wind energy in cold climates. International Energy Agency; 2003.

[2] Lehtomaki V. Emerging from the cold. Wind power monthly; 2016. https://www.windpowermonthly.com/article/1403504/emerging-cold?utm_source=website&utm_%20medium=social [accessed August 3, 2020].

[3] Seifert H. Technical requirements for rotor blades operating in cold climate. DEWI-Magazin; 2004.

[4] Battisti L, Dai Savio S, Dell'Anna S, Brighenti A. Evaluation of anti-icing energy and power requirement for wind turbine rotors in cold climates. Saariselkä, Findland: BOREAS VII, FMI; 2005.

[5] Buonocore JJ, Hughes EJ, Michanowicz DR, Heo J, Allen JG, Williams A. Climate and health benefits of increasing renewable energy deployment in the United States. Environ Res Lett 2019;14(11):114010. https://doi.org/10.1088/1748-9326/ab49bc.

[6] Lacroix A, Manwell J. Wind energy: cold weather issues. University of Massachusetts at Amherst, Renewable Energy Laboratory; 2000.

[7] Jordaens PJ, Krenn A, Wadham-Gagnon M, Davis N, Clausen N-E, Lehtomäki V, et al. IEA Wind Task 19 – Available technologies report of wind energy in cold climates; 2016.

[8] Battisti L. 14 – Optimising wind turbine design for operation in cold climates. In: Sørensen JD, Sørensen JN, editors. Wind Energy Systems. Elsevier; 2011. p. 388–460. https://doi.org/10.1533/9780857090638.3.388.

[9] Davis N. Icing impacts on wind energy production. DTU Wind Energy 2014.

[10] Zanon A, De Gennaro M, Kuhnelt H. Wind energy harnessing of the NREL 5 MW reference wind turbine in icing conditions under different operational strategies. Renewable Energy 2017;115:760–72. https://doi.org/10.1016/j.renene.2017.08.076.

[11] Lamraoui F, Fortin G, Benoit R, Perron J, Masson C. Atmospheric icing impact on wind turbine production. Cold Reg Sci Technol 2014;100:36–49. https://doi.org/10.1016/j.coldregions.2013.12.008.

[12] Dai J, Yang X, Wen L. Development of wind power industry in China: a comprehensive assessment. Renew Sustain Energy Rev 2018;97:156–64. https://doi.org/10.1016/j.rser.2018.08.044.

[13] Ahmed SD, Al-Ismail FSM, Shafiullah Md, Al-Sulaiman FA, El-Amin IM. Grid integration challenges of wind energy: a review. IEEE Access 2020;8:10857–78. https://doi.org/10.1109/ACCESS.2020.2964896.

[14] Notton G, Nivet M-L, Voyant C, Paoli C, Darras C, Motte F, et al. Intermittent and stochastic character of renewable energy sources: consequences, cost of intermittence and benefit of forecasting. Renew Sustain Energy Rev 2018;87:96–105. https://doi.org/10.1016/j.rser.2018.02.007.

[15] DeCesaro J, Porter K, Milligan M. Wind energy and power system operations: a review of wind integration studies to date. Electr J 2009;22(10):34–43. https://doi.org/10.1016/j.tej.2009.10.010.

[16] Wang X, Guo P, Huang X. A review of wind power forecasting models. Energy Procedia 2011;12:770–8. https://doi.org/10.1016/j.egypro.2011.10.103.

[17] WindSim. WindSim; n.d. http://www.windsim.com/ [accessed August 3, 2020].

[18] Thorsson P, Söderberg S, Bergström H. Modelling atmospheric icing: a comparison between icing calculated with measured meteorological data and NWP data. Cold Reg Sci Technol 2015;119:124–31. https://doi.org/10.1016/j.coldregions.2015.07.003.

[19] Sunden B, Wu Z. On icing and icing mitigation of wind turbine blades in cold climate. J Energy Resour Technol 2015;137(5). https://doi.org/10.1115/1.4030352.

[20] Davis N, Hahmann AN, Clausen N-E, Žagar M. Forecast of icing events at a wind farm in Sweden. J Appl Meteor Climatol 2014;53(2):262–81. https://doi.org/10.1175/JAMC-D-13-09.1.

[21] Davis NN, Pinson P, Hahmann AN, Clausen N-E, Žagar M. Identifying and characterizing the impact of turbine icing on wind farm power generation. Wind Energy 2016;19(8):1503–18. https://doi.org/10.1002/we.1933.

[22] Thompson G, Politovich MK, Rasmussen RM. A numerical weather model's ability to predict characteristics of aircraft icing environments. Wea Forecasting 2017;32(1):207–21. https://doi.org/10.1175/WAF-D-16-0125.1.

[23] Cattin R. Icing of wind turbines – Vindforsk projects, a survey of the development and research needs; 2012.

[24] Molinder J, Scher S, Nilsson E, Körnich H, Bergström H, Sjöblom A. Probabilistic forecasting of wind turbine icing related production losses using quantile regression forests. Energies 2020;14(1):158. https://doi.org/10.3390/en14010158.

[25] Yang X, Ye T, Wang Q, Tao Z. Diagnosis of blade icing using multiple intelligent algorithms. Energies 2020;13(11):2975. https://doi.org/10.3390/en13112975.

[26] Cheng X, Shi F, Liu X, Zhao M, Chen S. A novel deep class-imbalanced semisupervised model for wind turbine blade icing detection. IEEE Trans Neural Netw Learn Syst 2021:1–13. https://doi.org/10.1109/TNNLS.2021.3102514.

[27] Jiang W, Jin J. Intelligent icing detection model of wind turbine blades based on SCADA data. ArXiv:210707914 [Cs]; 2021.

[28] Shu L, Li H, Hu Q, Jiang X, Qiu G, McClure G, et al. Study of ice accretion feature and power characteristics of wind turbines at natural icing environment. Cold Reg Sci Technol 2018;147:45–54. https://doi.org/10.1016/j.coldregions.2018.01.006.

[29] Eolos Wind Research Station. Eolos Wind Energy Research; n.d. http://eolos.umn.edu/facilities/eolos-wind-research-station [accessed December 28, 2020].

[30] Savadjiev K, Farzaneh M. Study of icing rate and related meteorological parameter distributions during atmospheric icing events. In: Proceedings of the international offshore and polar engineering conference; 2001;1.

[31] Davis NN, Byrkjedal Ø, Hahmann AN, Clausen N-E, Žagar M. Ice detection on wind turbines using the observed power curve. Wind Energy 2016;19(6):999–1010. https://doi.org/10.1002/we.v19.610.1002/we.1878.

[32] Gao L, Hong J. Wind turbine performance in natural icing environments: a field characterization. Cold Regions 2021;181:103193. https://doi.org/10.1016/j.coldregions.2020.103193.

[33] Pourseif T, Afzalian A. Pitch angle control of wind turbine systems in cold weather conditions using mu robust controller. Int J Energy Environ Eng 2017;8:197–207. https://doi.org/10.1007/s40095-017-0231-y.

[34] Tabatabaei N. Impact of icing on wind turbines aerodynamic. Lulea University of Technology; 2018.

[35] Wind turbine. West Central Research and Outreach Center (WCROC) – Morris, MN; 2014. https://wcroc.cfans.umn.edu/research/renewable-energy/wind-turbine [accessed September 8, 2021].

[36] Chapter 3: WRF standard initialization (WPS); n.d. https://www2.mmm.ucar.edu/wrf/users/docs/user_guide_V3/user_guide_V3.9/users_guide_chap3.html [accessed September 8, 2021].

[37] Wang W, Gill D. Set up and run WRF (ARW-real); 2011.

[38] National Centers for Environmental Prediction/National Weather Service/NOAA/ U.S. Department of Commerce. NCEP GDAS/FNL 0.25 Degree global tropospheric analyses and forecast grids; 2015. https://doi.org/10.5065/D65Q4T4Z.

[39] Carvalho D, Rocha A, Gómez-Gesteira M, Silva SC. WRF wind simulation and wind energy production estimates forced by different reanalyses: comparison with observed data for Portugal. Appl Energy 2014;117:116–26. https://doi.org/10.1016/j.apenergy.2013.12.001.

[40] Tastula E-M, Vihma T. WRF model experiments on the Antarctic atmosphere in winter. Mon Wea Rev 2011;139(4):1279–91. https://doi.org/10.1175/2010MWR3478.1.

[41] Jeworrek J, West G, Stull R. WRF precipitation performance and predictability for systematically varied parameterizations over complex terrain. Weather Forecast 2021;36(3):893–913. https://doi.org/10.1175/WAF-D-20-0195.1.

[42] Gilliland EK, Rowe CM. A comparison of cumulus parameterization schemes in the WRF model. In: 87th AMS annual meeting, San Antonio, TX: University of Nebraska, Lincoln; 2007.

[43] Skamarock WC, Klemp JB, Dudhia J, Gill DO, Barker DM, Duda MG, et al. A description of the advanced research WRF version 3. Boulder, CO: National Center for Atmospheric Research; 2008.

[44] Jeworrek J, West G, Stull R. Evaluation of cumulus and microphysics parameterizations in WRF across the convective gray zone. Weather Forecast 2019; 34(4):1097–115. https://doi.org/10.1175/WAF-D-18-0178.1.

[45] Hong S-Y, Lim J-O-J. The WRF single-moment 6-class microphysics scheme (WSM6). J Kor Meteorol Soc 2006;42:129–51.

[46] Rasmussen RM, Vivekanandan J, Cole J, Myers B, Masters C. The estimation of snowfall rate using visibility. J Appl Meteorol 1999;38(10):1542–63.

[47] Fakorede O, Feger Z, Ibrahim H, Ilinca A, Perron J, Masson C. Ice protection systems for wind turbines in cold climate: characteristics, comparisons and analysis. Renew Sustain Energy Rev 2016;65:662–75. https://doi.org/10.1016/j.rser.2016.06.080.

[48] Deppe AJ, Gallus WA, Takle ES. A WRF ensemble for improved wind speed forecasts at turbine height. Wea Forecast 2013;28(1):212–28. https://doi.org/10.1175/WAF-D-11-00112.1.

[49] Misenis C. Meteorological model performance for annual 2016 simulation WRF v3.8. Research Triangle Park, NC: U.S. EPA – Office of Air Quality Planning and Standards; 2019.

[50] Shirey SM. A relative humidity based comparison of numerically modeled aerosol extinction to LIDAR and adiabatic parameterizations. Air Force Institute of Technology; 2016.

[51] Luo L, Zhang J. WRF-ice simulation on cyclone-induced blowing snow and associated physical processes over Antarctic peninsula. In: AGU fall meeting abstracts, vol. 44; 2019.

[52] Hoen B, Diffendorfer JE, Rand J, Kramer LA, Garrity CP, Roper AD, et al. United States wind turbine database; 2018. https://doi.org/10.5066/F7TX3DN0.

[53] HRRR model fields – experimental; n.d. https://rapidrefresh.noaa.gov/hrrr/HRRR/Welcome.cgi?dsKey=hrrr_ncep_jet [accessed January 13, 2021].

[54] National Centers for Environmental Prediction/Environmental Modeling Center. Weather research and forecast. EMC Home; n.d. https://www.emc.ncep.noaa.gov/emc/pages/infrastructure/wrf.php [accessed January 13, 2021].